

# Skyrmion Transport and Annihilation in Funnel Geometries

F. S. Rocha<sup>1</sup>, J. C. Bellizotti Souza<sup>1</sup>, N. P. Vizirim<sup>2</sup>, C. J. O. Reichhardt<sup>3</sup>, C. Reichhardt<sup>3</sup> and P. A. Venegas<sup>2</sup>

<sup>1</sup> POSMAT - Programa de Pós-Graduação em Ciência e Tecnologia de Materiais, Faculdade de Ciências, Universidade Estadual Paulista - UNESP, Bauru, SP, CP 473, 17033-360, Brazil

<sup>2</sup> Departamento de Física, Faculdade de Ciências, Unesp-Universidade Estadual Paulista, CP 473, 17033-360 Bauru, SP, Brazil

<sup>3</sup> Theoretical Division and Center for Nonlinear Studies, Los Alamos National Laboratory, Los Alamos, New Mexico 87545, USA

E-mail: nicolas.vizarim@unesp.br

**Abstract.** Using atomistic simulations, we have investigated the transport and annihilation of skyrmions interacting with a funnel array under a current applied perpendicular to the funnel axis. We find that transport without annihilation is possible at low currents, when the motion is dominated by skyrmion-skyrmion interactions and skyrmions push each other through the funnel opening. Skyrmion annihilation occurs for higher currents when skyrmions in the upper half of the sample exert pressure on skyrmions in the bottom half of the sample due to the external current. Upon interacting with the funnel wall, the skyrmions undergo a size reduction that makes it easier for them to pass through the funnel opening. We find five phases as a function of the applied current and the size of the funnel opening: (i) pinned, (ii) transport without annihilation, (iii) transport with annihilation, (iv) complete annihilation, and (v) a reentrant pinning phase that only occurs for very narrow openings. Our findings provide insight into how to control skyrmion transport using funnel arrays by delineating regimes in which transport of skyrmions is possible as well as the conditions under which annihilation occurs.

*Keywords:* Skyrmion, Transport, Information carrier, Hall angle, Annihilation

## 1. Introduction

Magnetic skyrmions are topologically protected particle-like spin configurations that have received growing attention in recent years. Due to their reduced size, stability, and ease of transport, skyrmions are considered to be a particularly promising candidate for creating new logical and memory spintronics devices [1, 2, 3]. Skyrmions arise in chiral magnetic materials [1, 4, 5] including MnSi, FeCoSi, and other B20 transition metal compounds [4, 6, 7, 5, 8], and their formation is the result of an interplay between the Dzyaloshinsky–Moriya (DM) interaction [9, 10] and ferromagnetic exchange.

One of the most important features of skyrmions is that they can be set into motion by the application of a transport current. It was shown that the current density needed to drive skyrmions is much lower than the currents necessary to move magnetic domain walls [11]. Thus, understanding skyrmion stability and behavior under the influence of transport currents is crucial for the creation of future technological devices. Due to their topology, skyrmions exhibit strong gyrotropic effects that strongly affect their dynamics [1, 12, 13]. In particular, under an applied spin current the skyrmions are deflected by the skyrmion Hall effect (SHE), which produces a finite skyrmion Hall angle  $\theta_{\text{sk}}^{\text{int}}$ . The magnitude of  $\theta_{\text{sk}}^{\text{int}}$  is determined by the material parameters along with intrinsic defects in the sample. In general,  $\theta_{\text{sk}}^{\text{int}}$  falls in the range  $0^\circ$  to  $55^\circ$  [13, 14, 15, 16], but larger values of  $\theta_{\text{sk}}^{\text{int}}$  are possible depending on the parameters of the system. For certain conditions that are related to non-adiabatic spin transfer torque, the Hall angle can be zero [17]. From a technological application point of view, a finite skyrmion Hall angle is problematic because it can cause the skyrmion to deviate towards the sample edge and annihilate, destroying any information that may have been associated with the skyrmion location. There have been various efforts to understand how to control the skyrmion motion and mitigate the intrinsic Hall angle, including through the use of periodic pinning [18, 19, 20, 21], ratchet effects [22, 23, 24, 25], 1D potential wells [26, 27, 28, 29, 30], nanotracks [31, 32], soliton motion [33], interface guided motion [34] and gradients in the strain, temperature, or magnetic field [35, 36, 37, 38].

Several proposals for skyrmion based devices involve using a skyrmion as the information carrier and controlling the flux of the skyrmions. In studies of skyrmions and racetrack memories, Zhang *et. al.* [39] not only showed the influence and importance of skyrmion-skyrmion interactions and the skyrmion-edge repulsion in racetracks, but also investigated the effect of spacing between consecutive skyrmionic bits and demonstrated the feasibility of writing, reading, and deleting skyrmions in future skyrmionic devices. Tomasello *et. al.* [40] analyzed scenarios for controlling Néel and Bloch skyrmions by SHE or spin-transfer torque (STT) and concluded that Néel skyrmions driven by SHE are more promising from a technological point of view since the skyrmion motion is less sensitive to the defects and edge roughness that are present in real skyrmion devices. These results pave the way for applications using skyrmions, such as a skyrmion diode, where skyrmions flow easily in one direction but not in the other. A typical method for reducing skyrmion flow in a given direction is to introduce a geometric constriction or obstacles for the skyrmions. Feng *et. al.* [41] proposed a stripe-shaped device with lateral asymmetry that allows the skyrmion to flow in the easy direction of the asymmetry but not in the hard direction. Skyrmions flowing along the easy direction follow the edge of the sample and can be transported through the device; however, a skyrmion that flows in the hard direction interacts with the lateral asymmetry and is annihilated. Using a similar idea, Jung *et. al.* [42] proposed a skyrmion diode involving asymmetrically shaped geometric structures. In this case, a skyrmion moving in the hard direction is not annihilated but becomes trapped, while skyrmions move readily in the easy direction. Recently, Bellizotti Souza *et.*

*al.* [43] designed a skyrmion diode device for multiple skyrmions based on an asymmetric funnel geometry where interacting skyrmions can become clogged. In the easy-flow direction of the funnel, the skyrmions move readily and the depinning current is very low; however, the depinning currents can be much higher for hard direction driving and reentrant pinning effects can occur in which flowing skyrmions cease to flow when the drive is increased. Overall, the skyrmion velocity is much larger for motion along the easy flow direction than along the hard flow direction, resulting in a diode effect for multiple skyrmions.

In this work, we use atomistic magnetic simulations to investigate the dynamics of multiple skyrmions moving through a periodic array of funnels constructed using spins with very strong perpendicular magnetic anisotropy (PMA). The funnel axes are aligned with the  $x$  direction and the transport current is applied along the  $-y$  direction. We find that for low currents, skyrmions can be transported along the funnel with no annihilation. As the applied current increases, the skyrmions exert pressure on each other that results in the onset of skyrmion annihilation. This annihilation produces free space inside the sample that reduces the amount of jamming occurring at the funnel tips and resulting in an increase in the average skyrmion velocity. We observe four distinct dynamic phases as a function of increasing current: (i) a pinned phase, (ii) motion without annihilation, (iii) motion with partial annihilation, and (iv) complete annihilation. The funnel opening plays a major role in the dynamics, with smaller openings hindering the skyrmion motion due to a strong bottleneck effect, while larger openings facilitate the skyrmion motion. By selecting the right combination of applied external current magnitude and funnel opening geometry, it is possible to produce a device that can rapidly transport skyrmions without annihilation.

## 2. Simulation

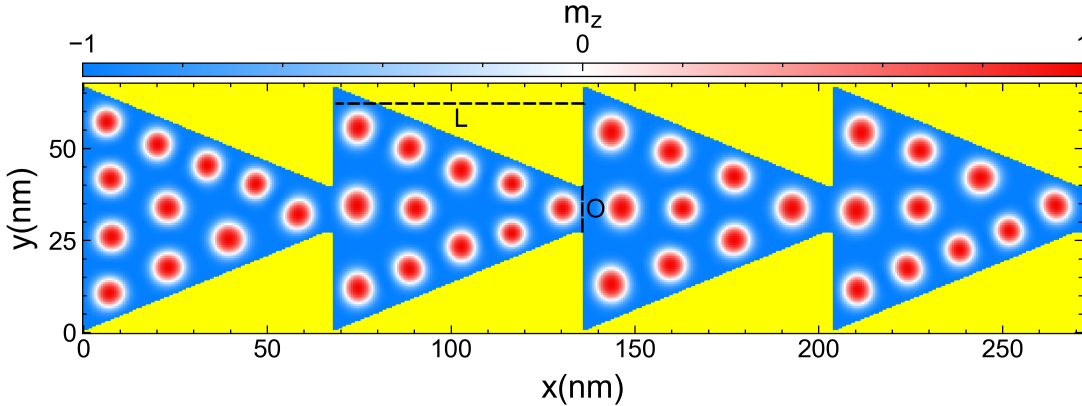


**Figure 1.** Image of the sample geometry. The funnel array is constructed by lining the upper and lower edges of the sample with an asymmetric sawtooth arrangement of rigid spins (yellow). The funnel has length  $L$  and opening size  $O$  as indicated in the figure. Inside the funnel, color ranging from blue to red indicates the magnitude of the out-of-plane magnetization  $m_z$ . Skyrmions are visible as red circles.

We simulate a ferromagnetic thin film that supports Néel skyrmions at  $T = 0\text{K}$  under the influence of a magnetic field applied along the  $z$  direction, perpendicular to the film plane. The

film has dimensions of 272 nm  $\times$  68 nm and contains rigid spins that form an asymmetric sawtooth arrangement running parallel to the  $x$  axis along the upper and lower edges of the film, as illustrated in Fig. 1. Each funnel plaquette has a length, in the  $x$  direction,  $L$  and opening  $O$ . Throughout the simulation we fix the funnel length as  $L = 68$  nm and vary  $O$ .

We use an atomistic model for the simulations [44] to investigate the skyrmion spin textures in detail. The following Hamiltonian governs the spin dynamics [45, 46, 47]:

$$\mathcal{H} = - \sum_{i,j \in N} J_{i,j} \mathbf{m}_i \cdot \mathbf{m}_j - \sum_{i,j \in N} \mathbf{D}_{i,j} \cdot (\mathbf{m}_i \times \mathbf{m}_j) - \sum_i \mu \mathbf{H} \cdot \mathbf{m}_i - \sum_i K_1 (\mathbf{m}_i \cdot \hat{\mathbf{z}})^2 \quad (1)$$

The first term on the right side is the exchange interaction between nearest neighbors, which compose the set  $N$ . Here, we consider a square lattice of spins with lattice constant  $a$  and exchange constant  $J_{i,j}$  between spins  $i$  and  $j$ . The second term is the Dzyaloshinskii-Moriya interaction, where  $\mathbf{D}_{i,j}$  is the Dzyaloshinskii-Moriya vector between spins  $i$  and  $j$  for thin films. The third term is the Zeeman interaction, with atomic magnetic moment  $\mu$ , and the last term is the sample easy-axis anisotropy where  $K_1$  is the anisotropy strength. We neglect long-range dipolar interactions since they are expected to be very small for ultrathin films[48]. The funnel walls are composed of rigid spins with  $\mathbf{m}_F = -\hat{\mathbf{z}}$  fixed over the set  $F$  of spins comprising the region outside the funnel. The rigid spins in magnetic walls are a simplified representation of spins with extremely high anisotropy. For example, if we replace the rigid spins by spins that have  $K_1 = 5J$ , we achieve the same results shown in this work.

The time evolution of the spins is given by the LLG equation augmented with the adiabatic spin-transfer torque (STT): [49, 50]:

$$\frac{d\mathbf{m}_i}{dt} = -\gamma \mathbf{m}_i \times \mathbf{H}_i^{\text{eff}} + \alpha \mathbf{m}_i \times \frac{d\mathbf{m}_i}{dt} + \frac{pa^3}{2e} (\mathbf{j} \cdot \nabla) \mathbf{m}_i \quad (2)$$

Here  $\gamma$  is the gyromagnetic ratio given by  $\gamma = g\mu_B/\hbar$ ,  $\mathbf{H}_i^{\text{eff}} = -\frac{1}{\mu} \frac{\partial \mathcal{H}}{\partial \mathbf{m}_i}$  is the effective field including all interactions of the Hamiltonian,  $\alpha$  is the Gilbert damping parameter, and the last term corresponds to the STT current, where  $p$  is the polarization,  $e$  is the electron charge,  $a$  is the lattice constant, and  $\mathbf{j}$  the applied current density. This is called the spin-transfer-torque term, and it includes the assumption that the conduction electron spins are parallel to the local magnetic moments  $\mathbf{m}$  [45, 51]. We do not include non-adiabatic spin transfer torque since it does not appreciably affect the dynamics of rigid nanoscale skyrmion quasiparticles at small driving forces [15]. We apply the current along the  $-y$  direction,  $\mathbf{j} = -j\hat{\mathbf{y}}$ . The direction was chosen based on the interaction of skyrmions with rigid magnetic walls that results in a boosted skyrmion velocity along the wall [29, 43, 52, 53, 54].

We measure the number of skyrmions in the sample using the topological charge, where each skyrmion gives a charge of  $Q = \pm 1$  depending on the direction of the applied field. Since we are considering a discrete lattice, the topological charge calculations are done using a lattice-based implementation, which is described in detail in Ref. [55]. Variations in the topological charge calculations due to inaccuracies in finite-difference derivatives can be reduced using the lattice-based approach, especially when nucleation, annihilation, and thermal fluctuations are considered.

The skyrmion velocities are calculated using the emergent electromagnetic field [11, 47]:

$$E_i^{\text{em}} = \frac{\hbar}{e} \mathbf{m} \cdot (\partial_i \mathbf{m} \times \partial_t \mathbf{m}) \quad , \quad B_i^{\text{em}} = \frac{\hbar}{2e} \varepsilon_{ijk} \mathbf{m} \cdot (\partial_j \mathbf{m} \times \partial_k \mathbf{m}) \quad (3)$$

where  $\varepsilon_{ijk}$  is the totally anti-symmetric tensor. The drift velocity  $\mathbf{v}_d$  is then computed according to  $\mathbf{E}^{\text{em}} = -\mathbf{v}_d \times \mathbf{B}^{\text{em}}$  [11, 47].

Throughout the simulation, we fix  $\alpha = 0.04$ ,  $p = -1.0$  and  $a = 0.5$  nm. We use the following material parameters:  $J = 1$  meV,  $D = 0.18J$ , and  $K_1 = 0.01J$ . The applied magnetic field is  $\mu\mathbf{H} = -0.5 (D^2/J) \hat{\mathbf{z}}$ , enabling the formation of a skyrmion phase [45, 47].

We initialize each simulation by placing randomized spin orientations throughout the sample that slowly stabilized into the described spin textures after several relaxation steps where we use the LLG equation without the spin current term ( $\mathbf{j} = \mathbf{0}$ ). We relax the system for  $3 \times 10^7$  time steps in order to guarantee that a steady solution has been reached. Once the initial state has been prepared, we introduce a finite spin current and begin to measure the dynamics of the system. For the calculations we use a Runge-Kutta fourth-order integration method was used where time is normalized by  $t = (\hbar/J)\tau$  and the spin current is given by  $\mathbf{j} = (2eJ/a^2\hbar)\mathbf{j}'$ . Here,  $\tau$  and  $\mathbf{j}'$  are the normalized dimensionless units from the code that are converted back to the correct dimension units.

### 3. Skyrmion Transport

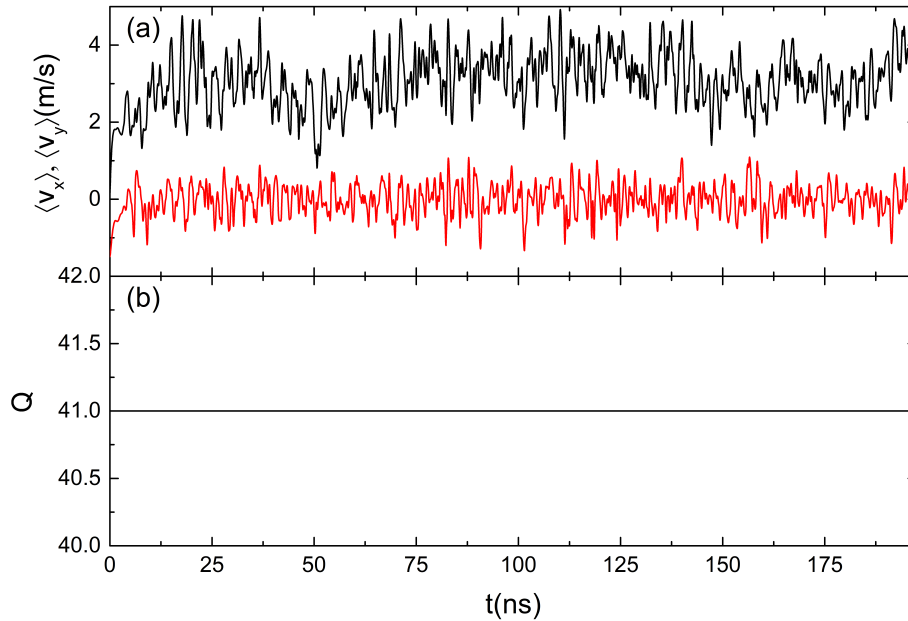


**Figure 2.** (a) Velocity signals  $\langle v_x \rangle$  (black) and  $\langle v_y \rangle$  (red) vs time  $t$  and (b) the corresponding topological charge  $Q$  vs  $t$  for a system with  $j = 0.39 \times 10^{10}$  A/m<sup>2</sup> and  $O = 12.5$  nm. Both  $\langle v_x \rangle$  and  $\langle v_y \rangle$  have noisy signatures. The velocity signal oscillates around  $\langle v_x \rangle \approx 3$  m/s and  $\langle v_y \rangle \approx 0$  m/s, signifying net motion along the  $x$  direction parallel to the funnel axis along with oscillations without net motion along the  $y$  direction. The topological charge  $Q = 41$  is constant throughout the simulation, indicating that no annihilation is occurring.

We first consider a system with funnel openings of size  $O = 12.5$  nm under an applied current of  $j = 0.39 \times 10^{10}$  A/m<sup>2</sup>, which is weak enough that no skyrmion annihilation occurs. In Fig. 2 we plot the skyrmion average velocities  $\langle v_x \rangle = |Q|^{-1} \sum_i^{|Q|} \mathbf{v}_d \cdot \hat{\mathbf{x}}$  and  $\langle v_y \rangle = |Q|^{-1} \sum_i^{|Q|} \mathbf{v}_d \cdot \hat{\mathbf{y}}$  along with the topological charge  $Q$  as a function of simulation time  $t$ . In Fig. 2(a), both velocity signals exhibit

a noisy behavior resulting from the skyrmion-skyrmion and skyrmion-wall interactions inside the funnel plaquettes. The skyrmions can deform in size inside the plaquettes, creating a turbulent motion with noisy velocity signatures at different average velocities of  $\langle v_x \rangle \approx 3$  m/s and  $\langle v_y \rangle \approx 0$  m/s. This indicates that the skyrmions undergo a net motion along the funnel array and travel from one funnel plaquette to the other along the  $x$  direction. In contrast, there is no net motion in the  $y$  direction but only oscillations in the skyrmion velocity. In Fig. 2(b), the topological charge is stabilized at  $Q = 41$ , indicating that 41 skyrmions are present in the sample and that there is no annihilation.

In Fig. 3 we show representative snapshots illustrating the skyrmion motion for the sample from Fig. 2. Since the external drive is applied along the  $-y$  direction, the skyrmions in the upper part of the funnels are larger and the skyrmions in the lower part of the funnels are smaller and more crowded. Compression of the skyrmions against the wall causes them to slide in the  $+x$  direction and slip through the funnel opening into the next plaquette to the right. The funnel opening presents a barrier for skyrmions on both the right and left sides of the opening, but skyrmions approaching from the left are able to jump over this barrier and move with high velocity into the neighboring plaquette. These skyrmions experience a bottleneck effect, as a result of which only one skyrmion can pass through the opening at a time. During the transition from one funnel plaquette to the other, the skyrmion deforms and shrinks in order to pass through the funnel opening. Interactions with the opening and other skyrmions generate excitations within the skyrmions, resulting in the noisy behavior found in Fig. 2. The skyrmions in the upper and lower corners of the funnel remain mostly immobile, undergoing deformations and oscillations but no net motion. The Supplemental Material includes a video illustrating the motion inside the funnels. The overall behavior is very similar to what was observed in Ref. [43], where a particle-based model was used to describe the jamming and clogging of skyrmions in funnel arrays. Due to the limitations of the particle model, skyrmion deformations, excitations, and annihilation were not included in the previous work. Here, we show in greater detail that skyrmion deformations produced by interactions with the magnetic walls and with other skyrmions generate internal excitations that result in the appearance of a noisy velocity signal.

#### 4. Skyrmion Annihilation

We next describe the influence of skyrmion annihilation on the skyrmion transport. When the applied current is low, skyrmions can move slowly along the funnel arrays and undergo deformation and jamming but no annihilation. In Fig. 4(a) we plot  $\langle v_x \rangle$  and  $\langle v_y \rangle$  versus  $t$  for a system with  $O = 12.5$  nm at a higher current of  $j = 1.36 \times 10^{10}$  A/m<sup>2</sup>, while in Fig. 4(b) we show the corresponding topological charge  $Q$  versus  $t$ . For  $t = 0$ , there are 41 skyrmions present and  $Q = 41$ , just as in Section 3 where no annihilation occurred. Here the current density is large enough that skyrmions begin to annihilate until a final steady value of  $Q = Q_f = 9$  is reached. The blue dashed line at  $t = 17$  ns marks the moment at which the annihilation process ends, indicated by the fact that the number of skyrmions in the sample remains constant. During the annihilation period, the velocity signal  $\langle v_x \rangle$  is generally increasing with time. This velocity increase results because the destruction of skyrmions increases the amount of free space inside each plaquette, decreasing the effectiveness of jamming and enabling greater skyrmion mobility along the  $x$  direction. There are two main drivers for skyrmion annihilation in our system. (i) Pressure from the applied current pushes the skyrmions toward the lower funnel wall. (ii) Skyrmions that are pushed by the drive also exert pressure on the skyrmions that are closest to the wall. The annihilation process is very

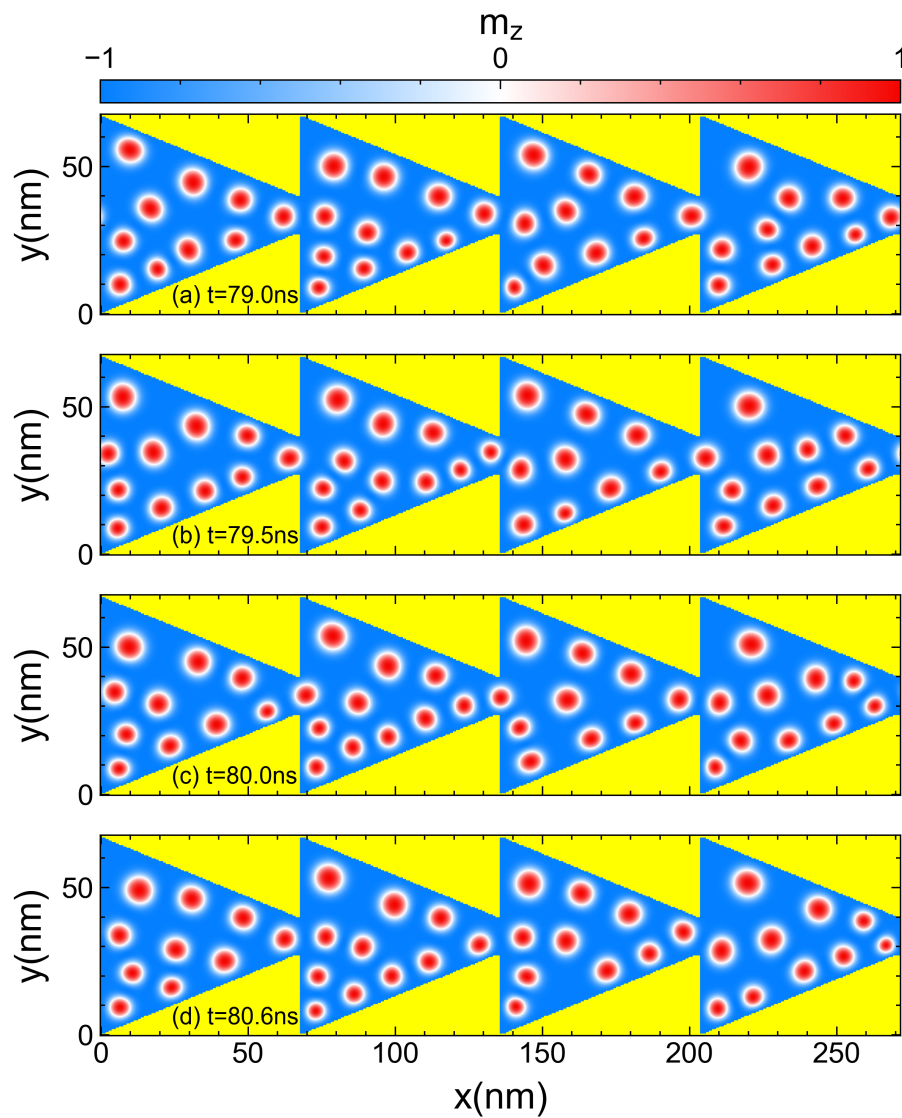


**Figure 3.** Snapshots of the skyrmion configurations at different times illustrating skyrmion motion through the funnel tips in a system with  $j = 0.39 \times 10^{10} \text{A/m}^2$  and  $O = 12.5 \text{ nm}$ . (a)  $t = 79.0 \text{ ns}$ . (b)  $t = 79.5 \text{ ns}$ . (c)  $t = 80.0 \text{ ns}$ . (d)  $t = 80.6 \text{ ns}$ .

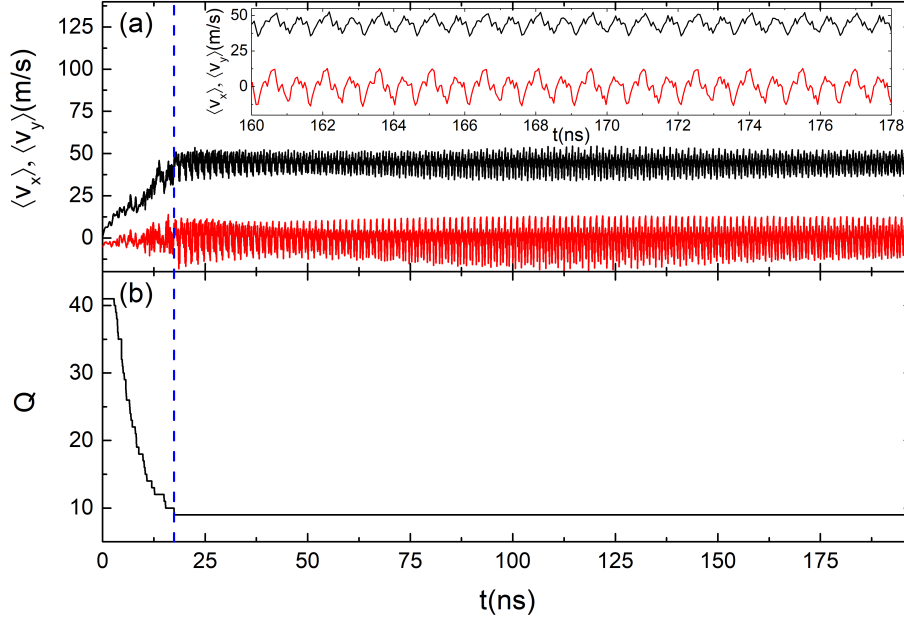


**Figure 4.** (a) Velocity signals  $\langle v_x \rangle$  (black) and  $\langle v_y \rangle$  (red) vs  $t$  and (b) the corresponding topological charge  $Q$  vs  $t$  for a system with  $j = 1.36 \times 10^{10}$  A/m<sup>2</sup> and  $O = 12.5$  nm. The blue dashed line at  $t = 17$  ns indicates the end of the annihilation process. The inset in panel (a) shows a detail of the velocity time series from the main panel.

similar to what has been observed recently for skyrmions interacting with magnetic walls [54], and consists of heavy deformation of the skyrmion followed by shrinking to annihilation. Since fewer skyrmions are present in the sample after the annihilation is complete, and these skyrmions have shrunk in size due to the pressure from the applied current, the remaining skyrmions are able to pass more easily through the funnel opening and the net velocity along the easy flow direction is increased. In addition, the surviving skyrmions interact strongly with the wall and experience a Magnus velocity boost [29, 56].

After the annihilation process has ended, the velocity no longer increases but instead exhibits a periodic signal, as highlighted in the inset of Fig 4(a) for the interval  $160 \leq t \leq 178$  ns. The velocity peaks at moments when most of the skyrmions are interacting with the lower walls of the funnel, where the Magnus boost effect can occur. Velocity minima occur each time a surviving skyrmion reaches the funnel tip and must overcome the barrier to reach the next plaquette. In this regime, the number of surviving skyrmions is sufficiently small that the skyrmion-skyrmion distance is large, rendering the interactions between skyrmions negligible and causing the behavior to be dominated by interactions with the walls, unlike what we observed in Section 3. The velocities oscillate around average values of  $\langle v_x \rangle \approx 45$  m/s and  $\langle v_y \rangle \approx 0$  m/s. The oscillation frequency depends on both the funnel size,  $L$  and the current density,  $j$ , with the frequency increasing for shorter funnels and decreasing for lower currents. Periodic behavior only occurs for systems in which each funnel plaquette hosts a steady state number of skyrmions that is small enough to allow all of the skyrmions to flow along the funnel wall, permitting interactions with the current and the wall to dominate over skyrmion-skyrmion interactions. Snapshots of the time evolution of



skyrmions undergoing periodic motion appear in Fig. 5, while the Supplemental Material includes a video illustrating the annihilation process for  $t < 17$  ns and the periodic skyrmion motion for  $t > 17$  ns.

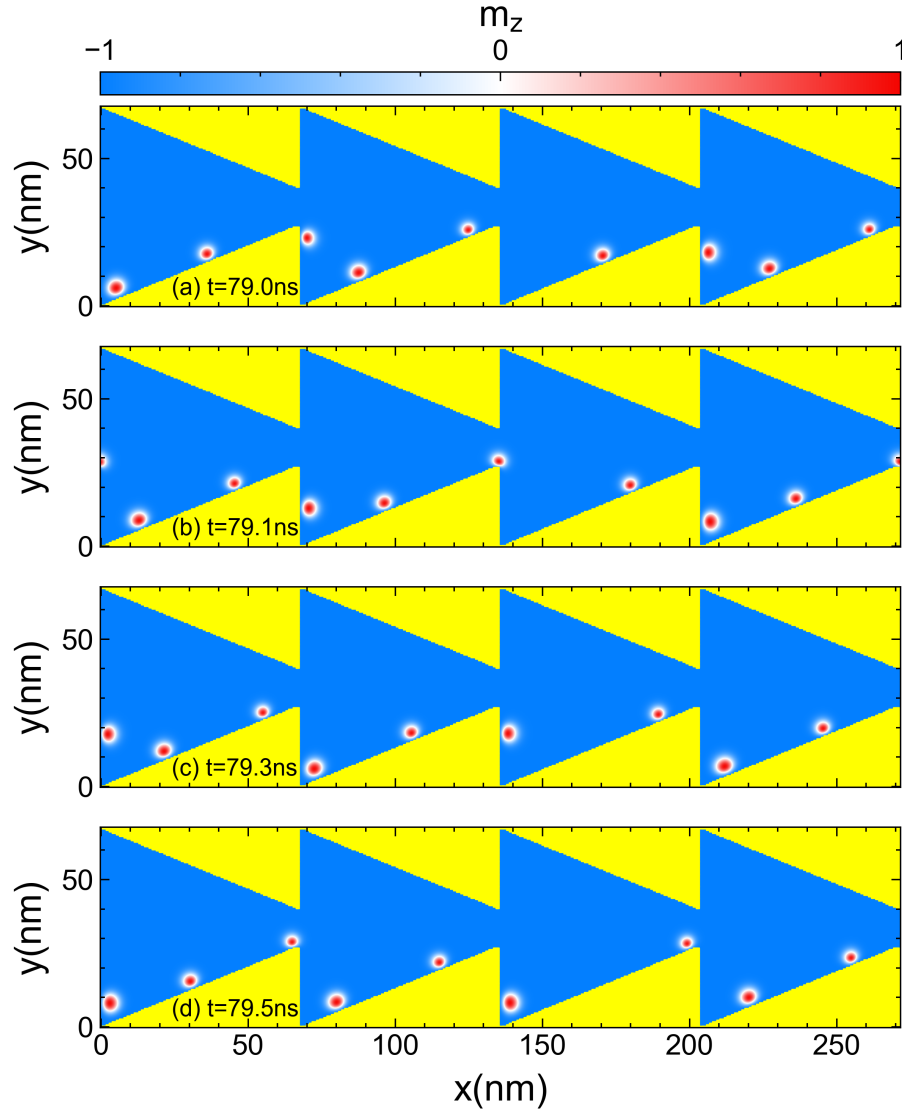


**Figure 5.** Snapshots of the skyrmion configurations at different times illustrating periodic skyrmion motion in the system containing  $Q_f = 9$  skyrmions with  $j = 1.36 \times 10^{10}$  A/m<sup>2</sup> and  $O = 12.5$  nm for times after the end of the annihilation process. (a)  $t = 79.0$  ns. (b)  $t = 79.1$  ns. (c)  $t = 79.3$  ns. (d)  $t = 79.5$  ns.

## 5. Transport Current

In the previous sections, we demonstrated that the applied current density can significantly affect the skyrmion behavior and determines whether annihilation processes occur. We next investigate in more detail how the magnitude of the current density can modify the skyrmion dynamics. We fix the funnel opening to  $O = 12.5$  nm and vary the applied current over the interval  $0.03 \times 10^{10} \text{ A/m}^2 \leq j \leq 1.58 \times 10^{10} \text{ A/m}^2$ .

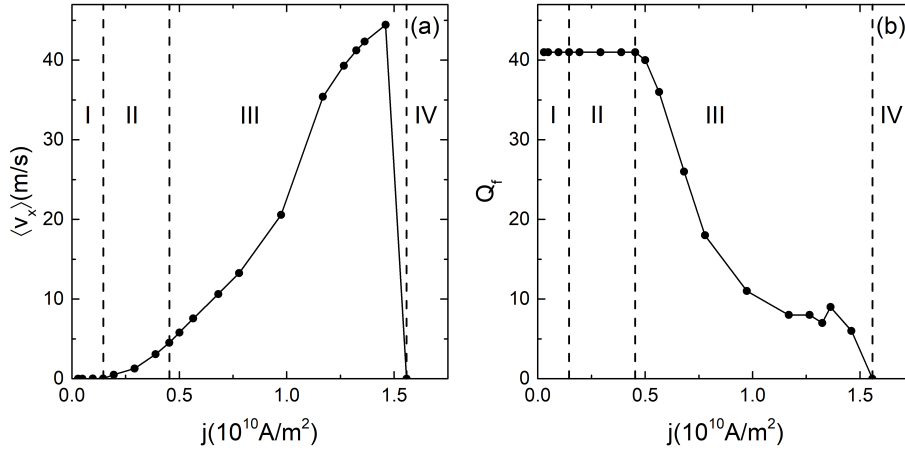


**Figure 6.** (a)  $\langle v_x \rangle$  and (b) final topological charge  $Q_f$  versus applied current  $j$  in a system with fixed funnel opening size  $O = 12.5$  nm. The dashed black lines indicate the boundaries of the four dynamic phases: I, no motion; II, motion without annihilation; III, motion with annihilation, and IV, complete annihilation of all skyrmions. There is a monotonic increase in  $\langle v_x \rangle$  with  $j$  until all of the skyrmions in the sample are annihilated, which occurs for  $j \geq 1.56 \times 10^{10} \text{ A/m}^2$ .  $Q_f$  exhibits a stable value in regions I and II, followed by a monotonic decrease with increasing  $j$  until  $Q_f = 0$ .

In Fig. 6(a) we plot  $\langle v_x \rangle$ , the velocity along the funnel axis, versus the applied current density  $j$ . We find a monotonic increase in  $\langle v_x \rangle$  with increasing applied current up to  $j = 1.45 \times 10^{10} \text{ A/m}^2$ . In the pinned region, labeled I, the skyrmions exhibit no net motion and are smoothly compressed against the wall. Region II, where motion without annihilation occurs, begins when the skyrmions depinning for  $j = 0.15 \times 10^{10} \text{ A/m}^2$ . The plot of the final topological charge  $Q_f$  versus  $j$  in Fig. 6(b) shows that in regions I and II, the topological charge remains constant at  $Q_f = 41$ . We note that at each value of  $j$ , the skyrmions are first initiated and stabilized in a sample with  $j = 0$ , and then the external drive is applied, which may modify the topological charge as shown in Fig. 4(b). Thus we report only the final stable topological charge value  $Q_f$  in Fig. 6(b). In region III, for  $j > 0.45 \times 10^{10} \text{ A/m}^2$ , the skyrmions are moving but an annihilation process occurs, and the number of skyrmions in the sample decreases with increasing  $j$ , resulting in a corresponding increase in the average skyrmion velocity. There are some small oscillations in the topological charge  $Q_f$  near  $j \approx 1.25 \times 10^{10} \text{ A/m}^2$ , but this is a result of the statistics of the small number of skyrmions present in the sample for these large currents. Increasing the current further causes the skyrmions to compress more strongly against bottom wall, shrinking the skyrmions and initiating the annihilation process described in detail in the previous section. The monotonic increase of  $\langle v_x \rangle$  with  $j$  in regions II and III is a consequence of the Magnus velocity boost effect caused by skyrmions

sliding along the wall. In region IV, for  $j > 1.45 \times 10^{10}$  A/m<sup>2</sup>, there is complete annihilation of all skyrmions in the sample and the skyrmion average velocity decreases sharply to zero.

## 6. Funnel Opening

Up until this point we have considered skyrmions interacting with a funnel array of fixed opening size  $O = 12.5$  nm. We next show how changing the opening size can significantly influence the dynamics since it controls the bottleneck effect. Smaller openings increase the bottleneck effect while larger openings reduce it, and thus, an understanding of how the funnel opening influences the skyrmion transport and annihilation processes through the bottleneck effect is essential to better understand the skyrmion dynamics. We vary the funnel opening over the range  $5 \text{ nm} \leq O \leq 25 \text{ nm}$  for applied currents ranging from  $0.03 \times 10^{10} \text{ A/m}^2 \leq j \leq 1.58 \times 10^{10} \text{ A/m}^2$ .

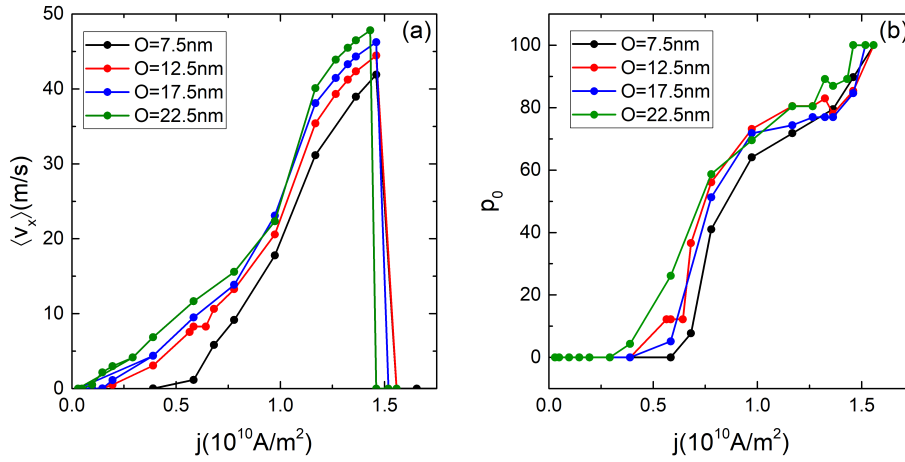


**Figure 7.** (a) Skyrmion average velocity  $\langle v_x \rangle$  and (b) the extinction probability  $p_0$  giving the percentage of skyrmions annihilated during the simulation vs applied current  $j$  for four different funnel opening sizes,  $O$ :  $O = 7.5$  nm (black),  $O = 12.5$  nm (red),  $O = 17.5$  nm (blue), and  $O = 22.5$  nm (green).

In Fig. 7 we plot the average velocity,  $\langle v_x \rangle$ , and the annihilation probability,  $p_0$  versus applied current density  $j$  for different funnel opening sizes. Here  $p_0$  describes the fraction of skyrmions originally present in the sample that are annihilated by the time steady state is reached. The general behavior of both  $\langle v_x \rangle$  and  $p_0$  is not changed when the funnel opening size is varied; instead, the values of  $j$  at which the different regions occur shifts, as  $O$  changes. The depinning threshold drops to lower values of  $j$  as  $O$  increases. For example, for  $O = 7.5$  nm, we find a depinning threshold of  $j = 0.39 \times 10^{10}$  A/m<sup>2</sup> that is much larger than the depinning threshold  $j = 0.05 \times 10^{10}$  A/m<sup>2</sup> of the  $O = 22.5$  nm sample. Smaller funnel openings enhance the bottleneck effect, making it necessary for more energy to be expended in order to deform the skyrmions enough to permit them to pass through the energy barrier separating adjacent plaquettes. As the funnel openings become larger, less energy is necessary to depin the skyrmions, leading to reduced depinning thresholds. Figure 7(b) shows the extinction probability  $p_0$  or the fraction of skyrmions annihilated during the simulation versus  $j$ . Minor differences appear as the funnel opening changes, but the general behavior remains the same. There is an annihilation-free plateau at low currents spanning regions

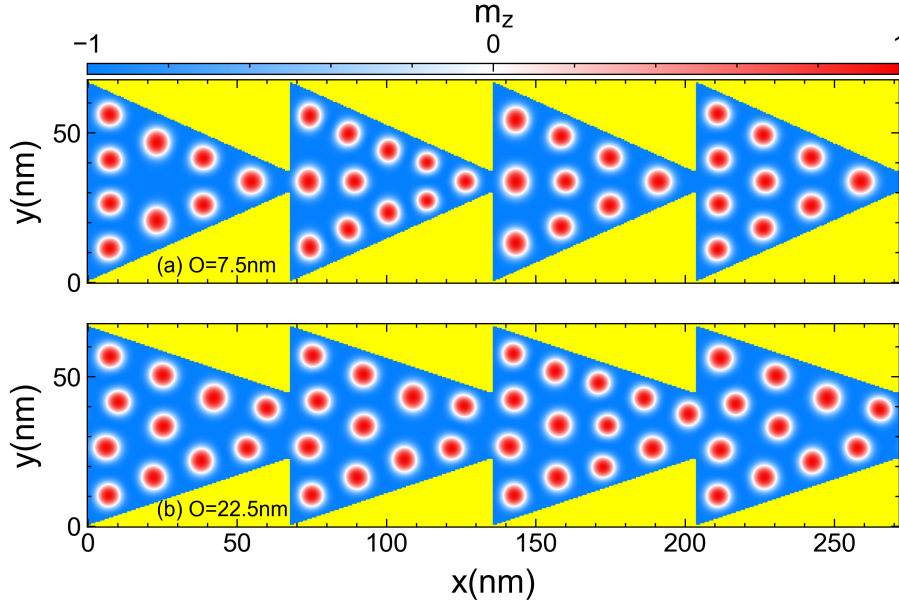


**Figure 8.** Snapshots of the skyrmion ground state configurations obtained after initializing the system with  $j = 0$  for different funnel opening sizes of (a)  $O = 7.5$  nm and (b)  $O = 22.5$  nm. In (a) there are  $Q = 39$  skyrmions and in (b) there are  $Q = 46$  skyrmions. Fewer skyrmions can be stabilized when the funnel opening size is reduced, which affects the dynamics once a current is applied.

I and II where the skyrmions either remain pinned or can flow while being conserved, followed by region III behavior of increasing annihilation up to complete skyrmion annihilation in region IV at high drives. The onset of the annihilation process shifts to lower values of  $j$  with increasing funnel opening size  $O$ . Larger funnel openings permit more skyrmions to remain stabilized in the sample since there is an expanded space for skyrmion motion and the applied magnetic field is held at a fixed value. In Fig. 8 we illustrate the skyrmion ground states obtained after initialization at  $j = 0$  for systems with  $O = 7.5$  nm and  $O = 22.5$  nm. For  $O = 22.5$  nm in Fig. 8(a), the wider funnel tips provide an increased space for accommodating skyrmions in the sample, resulting in the stabilization of  $Q = 46$  skyrmions. On the other hand, for  $O = 7.5$  nm, less space is available and only  $Q = 39$  skyrmions are stabilized. As a consequence, when an external drive is applied to the  $O = 22.5$  nm sample from Fig. 8(b), there is a greater compression of the skyrmions against the bottom wall of the funnel. This increased pressure favors enhanced skyrmion annihilation and a larger value of  $p_0$  when the funnel opening is large. In contrast, for the smaller  $O = 7.5$  nm funnel opening size in Fig. 8(a), the decrease in the number of stabilized skyrmions causes a corresponding decrease in the pressure exerted on the skyrmions adjacent to the lower funnel wall when a finite driving force is applied. Finally, when the funnel openings are larger, the orientation of the long funnel walls comes closer to being parallel to the  $x$  axis and perpendicular to the drive that is applied along the  $-y$  direction. This makes the lower funnel wall more effective at exerting pressure against the bottom row of driven skyrmions and lowers the threshold current at which skyrmion annihilation begins.

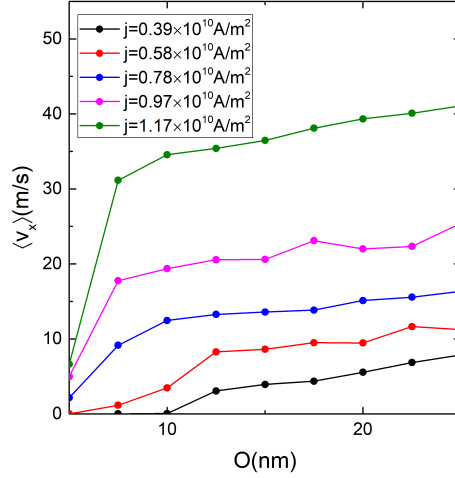


**Figure 9.**  $\langle v_x \rangle$  vs funnel opening size  $O$  for different applied currents of  $j = 0.39 \times 10^{10}$  A/m<sup>2</sup> (black),  $j = 0.58 \times 10^{10}$  A/m<sup>2</sup> (red),  $j = 0.78 \times 10^{10}$  A/m<sup>2</sup> (blue),  $j = 0.97 \times 10^{10}$  A/m<sup>2</sup> (magenta), and  $j = 1.17 \times 10^{10}$  A/m<sup>2</sup> (green).

In Fig. 9 we plot  $\langle v_x \rangle$  versus the funnel opening size  $O$  for selected values of the applied current in order to illustrate more clearly the skyrmion transport velocity is affected by the funnel opening size. We find that  $\langle v_x \rangle$  monotonically increases with increasing  $O$  for all values of the external drive  $j$ . The increase in  $\langle v_x \rangle$  is the most pronounced for small values of  $O$ , while  $\langle v_x \rangle$  tends toward a saturation value as  $O$  becomes large. This saturation value varies according to the magnitude of the current density, with larger currents giving larger saturation velocities. As the funnel openings become very large, the funnel structure itself begins to vanish, leading to the well studied case of skyrmions in a nanotrack [26, 29, 57]. For low applied currents, such as  $j = 0.39 \times 10^{10}$  A/m<sup>2</sup>, the skyrmions cannot be transported through the funnel opening when  $O \leq 10$  nm due to a strong jamming effect. As the applied current increases, this depinning threshold shifts to smaller values of  $O$ . For example, for  $j = 0.58 \times 10^{10}$  A/m<sup>2</sup>, the threshold depinning opening is around  $O = 5$  nm.

To summarize the general skyrmion transport behavior in funnel geometries, in Fig. 10 we plot a dynamic phase diagram as a function of applied current  $j$  versus funnel opening size  $O$ , where we highlight five regimes. Region I is the static or pinned phase where the skyrmions exhibit no net motion. It is present for all values of  $O$  considered in this work, but the depinning threshold generally decreases with increasing  $O$ . For small  $O$ , region I becomes more prominent due to the jamming of skyrmions produced by a strong bottleneck effect. In region II, skyrmions are transported along the funnels without annihilation, and the skyrmion number is conserved. This region appears only for a narrow window of current and disappears when  $O \leq 5$  nm. When  $O = 5$  nm, the funnel opening is too small to permit stable skyrmions to pass, and a skyrmion that tries to move from one funnel plaquette to another experiences such a strong compressive deformation that it annihilates rather than successfully translating to the next plaquette. Region III consists of skyrmion transport with partial annihilation. Here, the skyrmions can be transported through the funnels, but a fraction  $p_0 > 0$  of the skyrmions originally present are annihilated. This annihilation results primarily when the applied current produces pressure on the skyrmions along the bottom wall of the funnel, both

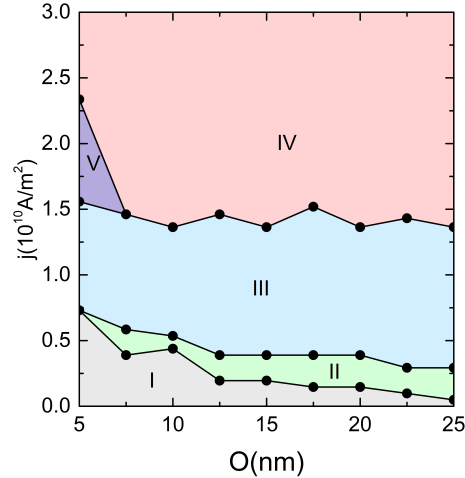


**Figure 10.** Dynamic phase diagram as a function of applied current  $j$  versus funnel opening size  $O$  highlighting five different regions. Region I (gray): no motion. Region II (green): motion without annihilation. Region III (light blue): motion with annihilation. Region IV (red): complete annihilation of all skyrmions. Region V (purple) is a reentrant pinned phase with no motion.

directly and as a result of compression from one or more layers of skyrmions that are not directly in contact with the bottom wall. This pressure causes the lower skyrmions to shrink, and eventually these skyrmions become so strongly deformed that they annihilate. In Region IV, we find complete annihilation of all skyrmions in the sample during transport. The threshold value of  $j$  at which this annihilation occurs is nearly independent of  $O$  and falls at  $j \approx 1.5 \times 10^{10}$  A/m<sup>2</sup>. This is expected because the critical current value that annihilates all skyrmions depends almost exclusively on the pressure exerted by the external drive and not on the angle of the long funnel walls or the strength of the skyrmion-skyrmion interactions. For very small funnel openings of  $O < 7.5$  nm, we find a reentrant pinned state marked region V. In this regime, skyrmions begin to annihilate when a drive is applied, but when only a few skyrmions remain in the sample, they become unable to pass through the small opening separating neighboring plaquettes, resulting in a stable pinned configuration. For these small funnel openings, the skyrmion transport from one funnel to the next is primarily driven by collective skyrmion interactions, where each skyrmion pushes its neighboring skyrmion through the funnel tip in a chain reaction process. When the current reaches the lower boundary of region V, most of the skyrmions in the sample are annihilated and this collective motion is destroyed, trapping the skyrmions in individual funnel plaquettes.

## 7. Summary

Using atomistic simulations, we investigated the dynamical behavior of skyrmions interacting with a funnel geometry. Under different currents applied along the  $-\hat{y}$  direction, perpendicular to the funnel axis. We find that skyrmions can be transported through the funnel openings due to a combination of Magnus force and collective effects. For driving currents just above the depinning threshold, the skyrmions can be transported without annihilation. For intermediate drive, the skyrmions continue to move but some skyrmions are destroyed in an annihilation process that

results from skyrmion-wall and skyrmion-skyrmion interactions. The external current causes the skyrmions in the upper part of the funnel to exert pressure on the skyrmions along the bottom of the funnel, which shrink to the point that they eventually annihilate. As more skyrmions are annihilated, the collective interactions are reduced and the remaining skyrmions move more freely through the funnels. Under large drives of  $j \approx 1.5 \times 10^{10}$  A/m<sup>2</sup>, the pressure from the driving current is too strong and all of the skyrmions in the sample are annihilated.

We demonstrate that the size of the funnel opening plays a major role in the dynamics. It takes more energy to force skyrmions through small funnel openings since the skyrmions must deform significantly in order to squeeze through the opening, and as a result the onset of skyrmion motion shifts to higher currents as the funnel openings decrease in size. For larger funnel openings, the skyrmions deform less and require less energy to pass through the opening. The onset of the annihilation process also shifts to lower current values as the funnel opening size increases. Larger funnel openings provide a greater amount of space in which more skyrmions can be stabilized at zero current since we hold the applied magnetic field fixed. When a current is then applied, the increased skyrmion density in funnels with large openings increases the current-induced pressure exerted by skyrmions in the upper part of the sample on skyrmions along the lower funnel wall. As a result, the annihilation threshold drops to lower applied currents in systems with larger funnel openings.

Our findings provide new insights into the role of collective effects, dynamics, and annihilation processes for skyrmions in nanodevices that could be used in future technological applications. Our results will be of use in developing new ways to transport skyrmions, permitting the skyrmions to carry information in a controlled manner.

## Acknowledgements

This work was supported by the US Department of Energy through the Los Alamos National Laboratory. Los Alamos National Laboratory is operated by Triad National Security, LLC, for the National Nuclear Security Administration of the U. S. Department of Energy (Contract No. 892333218NCA000001). J.C.B.S and N.P.V acknowledge funding from Fundação de Amparo à Pesquisa do Estado de São Paulo - FAPESP (Grants 2022/14053-8 and 2017/20976-3 respectively). We would like to thank Dr. Felipe F. Fanchini for providing the computational resources used in this work. These resources were funded by the Fundação de Amparo à Pesquisa do Estado de São Paulo - FAPESP (Grant: 2021/04655-8).

## References

- [1] Nagaosa N and Tokura Y 2013 *Nature Nanotechnol.* **8** 899–911
- [2] Everschor-Sitte K, Masell J, Reeve R M and Kläui M 2018 *Journal of Applied Physics* **124** 240901
- [3] Fert A, Reyren N and Cros V 2017 *Nature Rev. Mater.* **2** 1–15
- [4] Mühlbauer S, Binz B, Jonietz F, Pfleiderer C, Rosch A, Neubauer A, Georgii R and Böni P 2009 *Science* **323** 915–919
- [5] Yu X Z, Onose Y, Kanazawa N, Park J H, Han J H, Matsui Y, Nagaosa N and Tokura Y 2010 *Nature* **465** 901–904
- [6] Münzer W, Neubauer A, Adams T, Mühlbauer S, Franz C, Jonietz F, Georgii R, Böni P, Pedersen B, Schmidt M, Rosch A and Pfleiderer C 2010 *Physical Review B* **81** 041203
- [7] Pfleiderer C, Adams T, Bauer A, Biberacher W, Binz B, Birkelbach F, Böni P, Franz C, Georgii R, Janoschek M, Jonietz F, Keller T, Ritz R, Mühlbauer S, Münzer W, Neubauer A, Pedersen B and Rosch A 2010 *Journal of Physics: Condensed Matter* **22** 164207

- [8] Yu X Z, Kanazawa N, Onose Y, Kimoto K, Zhang W Z, Ishiwata S, Matsui Y and Tokura Y 2011 *Nature Materials* **10** 106–109
- [9] Dzyaloshinsky I 1958 *Journal of Physics and Chemistry of Solids* **4** 241–255
- [10] Moriya T 1960 *Physical Review* **120** 91–98
- [11] Schulz T, Ritz R, Bauer A, Halder M, Wagner M, Franz C, Pfleiderer C, Everschor K, Garst M and Rosch A 2012 *Nature Phys.* **8** 301–304
- [12] Reichhardt C, Reichhardt C J O and Milosevic M 2022 *Rev. Mod. Phys.* **94** 035005
- [13] Jiang W, Zhang X, Yu G, Zhang W, Wang X, Jungfleisch M B, Pearson J E, Cheng X, Heinonen O, Wang K L, Zhou Y, Hoffmann A and te Velthuis S G E 2017 *Nature Phys.* **13** 162–169
- [14] Reichhardt C, Ray D and Reichhardt C J O 2015 *Phys. Rev. Lett.* **114**(21) 217202
- [15] Litzius K, Lemesh I, Krüger B, Bassirian P, Caretta L, Richter K, Büttner F, Sato K, Tretiakov O A, Förster J, Reeve R M, Weigand M, Bykova I, Stoll H, Schütz G, Beach G S D and Kläui M 2017 *Nature Phys.* **13** 170–175
- [16] Zeissler K, Finizio S, Barton C, Huxtable A J, Massey J, Raabe J, Sadovnikov A V, Nikitov S A, Brearton R, Hesjedal T, van der Laan G, Rosamond M C, Linfield E H, Burnell G and Marrows C H 2020 *Nature Commun.* **11** 428
- [17] Zhang X, Xia J, Zhao G P, Liu X and Zhou Y 2017 *IEEE Transactions on Magnetics* **53** 1–6
- [18] Reichhardt C, Ray D and Reichhardt C J O 2015 *Physical Review B* **91** 104426
- [19] Ma F, Reichhardt C, Gan W, Reichhardt C J O and Lew W S 2016 *Phys. Rev. B* **94**(14) 144405
- [20] Vizarim N P, Reichhardt C, Reichhardt C J O and Venegas P A 2020 *New Journal of Physics* **22** 053025
- [21] Feilhauer J, Saha S, Tobik J, Zelent M, Heyderman L J and Mruczkiewicz M 2020 *Physical Review B* **102** 184425
- [22] Göbel B and Mertig I 2021 *Sci. Rep.* **11** 3020
- [23] Reichhardt C, Ray D and Reichhardt C J O 2015 *New J. Phys.* **17** 073034
- [24] Yamaguchi R, Yamada K and Nakatani Y 2020 *Japan. J. Appl. Phys.* **60** 010904
- [25] Souza J C B, Vizarim N P, Reichhardt C J O, Reichhardt C and Venegas P A 2021 *Phys. Rev. B* **104** 054434
- [26] Purnama I, Gan W L, Wong D W and Lew W S 2015 *Scientific Reports* **5** 10620
- [27] Reichhardt C and Reichhardt C J O 2016 *Phys. Rev. B* **94**(9) 094413
- [28] González-Gómez L, Castell-Queralt J, Del-Valle N, Sanchez A and Navau C 2019 *Phys. Rev. B* **100**(5) 054440
- [29] Juge R, Bairagi K, Rana K G, Vogel J, Sall M, Mailly D, Pham V T, Zhang Q, Sisodia N, Foerster M, Aballe L, Belmeguenai M, Roussigné Y, Auffret S, Buda-Prejbeanu L D, Gaudin G, Ravelosona D and Boulle O 2021 *Nano Lett.* **21**(7) 2989–2996
- [30] Del-Valle N, Castell-Queralt J, González-Gómez L and Navau C 2022 *APL Mater.* **10** 010702
- [31] Zhang X, Ezawa M and Zhou Y 2015 *Scientific Reports* **5** 9400
- [32] Toscano D, Mendonça J P A, Miranda A L S, Araujo C I L, Sato F, Coura P Z and Leonel S A 2020 *Journal of Magnetism and Magnetic Materials* **504** 166655
- [33] Vizarim N P, Souza J C B, Reichhardt C J O, Reichhardt C, Milošević M V and Venegas P A 2022 *Physical Review B* **105** 224409
- [34] Vizarim N P, Reichhardt C, Venegas P A and Reichhardt C J O 2021 *J. Mag. Mag. Mater.* **528** 167710
- [35] Yanes R, Garcia-Sanchez F, Luis R F, Martinez E, Raposo V, Torres L and Lopez-Diaz L 2019 *Applied Physics Letters* **115** 132401
- [36] Zhang S L, Wang W W, Burn D M, Peng H, Berger H, Bauer A, Pfleiderer C, van der Laan G and Hesjedal T 2018 *Nature Communications* **9** 2115
- [37] Everschor K, Garst M, Binz B, Jonietz F, Mühlbauer S, Pfleiderer C and Rosch A 2012 *Physical Review B* **86** 054432
- [38] Kong L and Zang J 2013 *Physical Review Letters* **111** 067203
- [39] Zhang X, Zhao G P, Fangohr H, Liu J P, Xia W X, Xia J and Morvan F J 2015 *Scientific Reports* **5** 7643
- [40] Tomasello R, Martinez E, Zivieri R, Torres L, Carpentieri M and Finocchio G 2015 *Scientific Reports* **4** 6784
- [41] Feng Y, Zhang X, Zhao G and Xiang G 2022 *IEEE Trans. Electron Devices* **69** 1293
- [42] Jung D H, Han H S, Kim N, Kim G, Jeong S, Lee S, Kang M, Im M Y and Lee K S 2021 *Phys. Rev. B* **104**(6) L060408
- [43] Souza J C B, Vizarim N P, Reichhardt C J O, Reichhardt C and Venegas P A 2022 *New J. Phys.* **24** 103030
- [44] Evans R F L 2018 *Atomistic Spin Dynamics Handbook of Materials Modeling: Applications: Current and Emerging Materials* ed Andreoni W and Yip S (Springer International Publishing) pp 1–23
- [45] Iwasaki J, Mochizuki M and Nagaosa N 2013 *Nature Commun.* **4** 1463
- [46] Iwasaki J, Mochizuki M and Nagaosa N 2013 *Nature Nanotechnology* **8** 742–747
- [47] Seki S and Mochizuki M 2016 *Skyrmions in Magnetic Materials* SpringerBriefs in Physics (Springer International Publishing)



- [48] Paul S, Haldar S, von Malottki S and Heinze S 2020 *Nature Communications* **11** 4756
- [49] Gilbert T 2004 *IEEE Transactions on Magnetics* **40** 3443–3449
- [50] Slonczewski J C 1996 *Journal of Magnetism and Magnetic Materials* **159** L1–L7
- [51] Zang J, Mostovoy M, Han J H and Nagaosa N 2011 *Physical Review Letters* **107** 136804
- [52] Zhang X, Xia J and Liu X 2022 *Physical Review B* **105** 184402
- [53] Zhang X, Xia J and Liu X 2022 *Physical Review B* **106** 094418
- [54] Bellizotti Souza J C, Vizarim N P, Reichhardt C J O, Reichhardt C and Venegas P A 2023 *New Journal of Physics* **25** 053020 ISSN 1367-2630
- [55] Kim J V and Mulkers J 2020 *IOP SciNotes* **1** 025211
- [56] Bellizotti Souza J, Vizarim N, Olson Reichhardt C J, Reichhardt C and Venegas P 2022 *Journal of Physics: Condensed Matter*
- [57] Sampaio J, Cros V, Rohart S, Thiaville A and Fert A 2013 *Nature Nanotechnology* **8** 839–844